JOURNAL OF APPLIED PHYSICS VOLUME 95, NUMBER 12 15 JUNE 2004

Phase transformation dynamics during welding of Ti–6Al–4V

J. W. Elmer[a] and T. A. Palmer
Lawrence Livermore National Laboratory, Livermore, California 94551

S. S. Babu
Oak Ridge National Laboratory, Oak Ridge, Tennessee 37831

W. Zhang and T. DebRoy
The Pennsylvania State University, University Park, Pennsylvania 16802

(Received 18 November 2003; accepted 15 March 2004)

In situ time-resolved x-ray diffraction (TRXRD) experiments were used to track the evolution of the $\alpha \rightarrow \beta \rightarrow \mathrm{L} \rightarrow \beta \rightarrow \alpha/\alpha'$ phase transformation sequence during gas tungsten arc welding of Ti–6Al–4V. Synchrotron radiation was employed for the *in situ* measurements in both the fusion zone (FZ) and the heat-affected zone (HAZ) of the weld, providing information about transformation rates under rapid heating and cooling conditions. The TRXRD data were coupled with the results of computational thermodynamic predictions of phase equilibria, and numerical modeling of the weld temperatures. The results show that significant superheat is required above the β transus temperature to complete the $\alpha \rightarrow \beta$ transformation during weld heating, and that the amount of superheat decreases with distance from the center of the weld where the heating rates are lower. A Johnson–Mehl–Avrami phase transformation model yielded a set of kinetic parameters for the prediction of the $\alpha \rightarrow \beta$ phase transformation during weld heating. Corresponding TRXRD measurements were made during weld cooling. In the HAZ, the $\beta \rightarrow \alpha$ transformation during weld cooling was shown to initiate at the β transus temperature and terminate below the Ms temperature, resulting in a microstructure containing a substantial fraction of α' martensite. In the FZ, the $\beta \rightarrow \alpha$ transformation during weld cooling was shown to initiate below the Ms temperature, and to completely transform the microstructure to α' martensite. © *2004 American Institute of Physics.* [DOI: 10.1063/1.1737476]

I. INTRODUCTION

Ti–6Al–4V is one of the most commonly used titanium alloys due to its favorable combination of physical and mechanical properties.[1–3] This alloy is oftentimes thermomechanically treated to produce a desired amount of equiaxed α (hcp crystal structure) and intergranular β (bcc crystal structure) with a fine grain size for optimum mechanical properties. However, microstructural changes such as annealing, recrystallization, and phase transformation to the high-temperature β phase during welding alter the grain size, phase ratios, and microstructural morphologies in the weld region.[4] The degree to which the microstructure is altered depends on the weld thermal cycles experienced at a particular location, and the kinetics of the various phase transformations taking place there. Although the weld thermal cycles can be calculated with a high degree of confidence using existing numerical models, the same is not true for the phase transformation kinetics under actual welding conditions.

In order to understand the transformation kinetics, the crystal structure of Ti–6Al–4V was directly observed during welding using a time-resolved x-ray diffraction (TRXRD) technique. This technique is used to make dynamic observations of microstructural evolution in both the fusion zone (FZ) and heat-affected zone (HAZ) of welds.[5–7] To do this, the spatially resolved x-ray beam was positioned at different locations relative to the center of the Ti–6Al–4V weld, as discussed in greater detail later. These different locations allowed the *in situ* TRXRD experiments to track both the $\alpha \rightarrow \beta$ and the $\beta \rightarrow \alpha$ transformations at different heating and cooling rates. In addition, the peak temperatures experienced at each location were different, producing microstructures that showed the increased effects of temperature at locations closer to the center of the weld.

Of particular interest to this investigation was the effect that the degree of transformation during weld heating had on the subsequent reverse transformation that occurred during cooling. The microstructural effects important to the cooling transformations were shown to be grain size, chemical homogenization, and the degree of the $\alpha \rightarrow \beta$ transformation just before the welding arc was terminated. Since each of these factors increases in severity towards the center of the weld, the TRXRD measurements made at different weld locations were able to directly observe these effects.

Analysis of the TRXRD experimental data was accomplished with the aid of computational thermal fluids modeling to calculate weld temperatures, and computational thermodynamics to calculate key phase transformation temperatures. By combining the computed temperatures with the TRXRD data, the kinetics of the phase transformations in Ti–6Al–4V could be determined. This allowed the $\alpha \rightarrow \beta$ transformation on heating to be quantified so that the degree

---

[a] Electronic mail: elmer1@llnl.gov

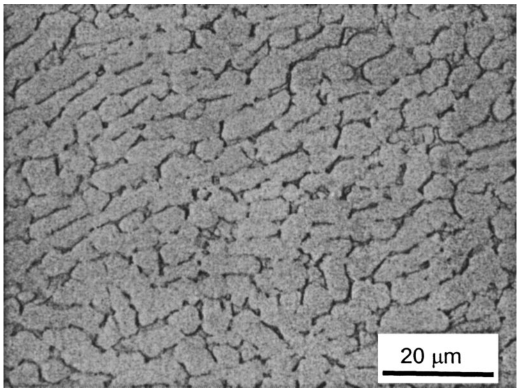

FIG. 1. Base metal microstructure, showing intergranular β outlining the α grains.

of transformation could be predicted throughout the weld HAZ, and thus aid in the prediction of the important phase transformations that occur during weld cooling.

Results of this investigation show that a significant amount of superheating is required to transform the microstructure on weld heating, and that partially transformed regions exist in the HAZ relatively close to the fusion zone boundary. Furthermore, martensite was observed to form during cooling, and the amount of martensite that formed was shown to be influenced by the grain size and completeness of the transformed microstructure at the initiation of the cooling cycle. These differences led to the observed differences in the postweld microstructure between the FZ and HAZ locations.

II. EXPERIMENTAL PROCEDURES

A. Materials and welding

Ti–6Al–4V ELI (extra low interstitial) was acquired in a 114 mm diameter bar. Samples 100 mm in diameter and 75 mm in length were machined from the bar for the TRXRD experiments. Chemical analysis of the starting material gave its composition to be: 6.0 Al, 4.2 V, 0.11 O, 0.17 Fe, 0.0028 H, 0.014 C, 0.009 N, 0.03 Si, bal. Ti (by wt %). Figure 1 shows the microstructure of the starting material, which contains approximately 12% β distributed intergranularly around the slightly elongated α grains that form the matrix. The α grains of the starting material have an aspect ratio of approximately 2:1, with an average grain size of 5.8 μm across the small dimension of the grains.

Gas tungsten arc spot welds were made on the Ti–6Al–4V alloy bars by striking a stationary arc, maintaining this arc for a fixed amount of time, then extinguishing the arc to let the weld cool. TRXRD data were gathered over a period of 60 s during welding, allowing both the heating and cooling cycles to be observed during one weld. Three different experimental conditions were investigated by positioning the x-ray beam at three locations. At the first location (4.5 mm from the weld center), the temperature–time profile of the weld was sufficient to melt and resolidify the alloy. At the second location (5.0 mm from the weld center) the time–temperature profile was sufficient to completely transform the alloy to the high-temperature β phase during heating. At the third location (5.5 mm from the weld center) the time–temperature profile was only capable of producing a partial transformation to the β phase during heating. The welding parameters used in this study are summarized in Table I, and produced weld pools 10 mm in diameter.

All of the welds were made inside an environmentally controlled chamber that was backfilled with high-purity helium to deliver the x-ray beam with minimal attenuation, and to prevent oxidation of the titanium alloy surface that would otherwise occur during welding. In addition, a cross jet of helium gas was directed at the x-ray beam impingement location to prevent metal vapors from depositing on the surface where x-ray diffraction was taking place. After the TRXRD experiments were completed, metallographic inspection was performed by sectioning and polishing the welds using standard metallographic procedures. The samples were then chemically etched using a solution containing 5 ml HF, 10 ml HNO_3, 30 ml lactic acid for approximately 30 s to reveal the base metal and weld microstructures. Remmington B etchant (10 ml HF, 10 ml glycol for approximately 1 min) was used to reveal the fusion zone boundary.

Microchemical compositions of the starting α and β phases were determined using microprobe analysis. The data were collected on a JEOL-8200 microprobe, operating at 15 KV and a beam current of 20 nA. Individual point locations were inspected using a beam diameter of 1 μm, while ''broad beam'' analysis was obtained by rastering a 1 μm beam over a 100×100 μm raster. X-ray intensities were calibrated using Ti, V, Al, Fe, and SiO_2 for oxygen, and corrected to wt % using the ZAF corrections. The intensities were also run using TiO_2 and Al_2O_3 as standards and yielded results within error of those calibrated using Ti and Al. Results of the microchemical analysis of each phase in the starting material are shown in Table II. These compositions represent the average of seven locations for each phase, and the estimated error corresponds to a 1 σ variation about the mean. It is clear from these results that V and Fe partition to

TABLE I. Summary of welding parameters used during the TRXRD experiments, and the location of the x-ray beam with respect to the center of the weld.

Weld	Average current (amp)	Voltage (V)	Arc on time (s)	X-ray location from weld center (mm)	Comments
1	100	19	20	4.5	Fusion zone
2	100	19	17	5.0	Fully transformed to β
3	100	19	17	5.5	Partially transformed to β

TABLE II. Chemical composition of the α and β phases in the base metal as measured by microprobe analysis. Seven points were averaged into each composition and the 1σ value is given as the estimated error.

	Al	V	Fe	Ti
Nominal composition	6.2	4.0	0.17	92.5
β phase	2.92 ± 0.11	15.43 ± 0.86	1.32 ± 0.11	80.7 ± 0.70
α phase	6.73 ± 0.33	1.42 ± 0.73	0.04 ± 0.02	91.2 ± 0.47

the β phase, while Al partitions to the α phase. In addition to the microchemical composition information, backscattered electron images of the polished surface were used to show the initial area fraction of β in the microstructure to be 12.1%.

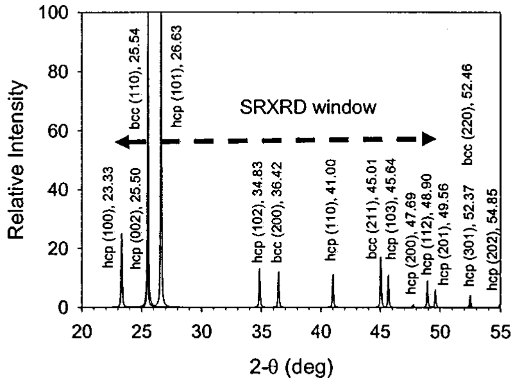

FIG. 3. Calculated locations of the β-Ti (bcc) and α-Ti (hcp) peaks that can appear from 20° to 55° of 2θ at 12.0 keV. The 2θ window of the x-ray detector is indicated by the horizontal dashed line.

B. Time-resolved x-ray diffraction

TRXRD measurements were performed on a 31-pole wiggler beamline (10-2) at the Stanford Synchroton Radiation Laboratory (SSRL) with SPEAR (Stanford Positron Electron Accumulation Ring) operating at an electron energy of 3.0 GeV and an injection current of ~100 mA.[8] Details of similar welding experiments have been previously published for titanium,[9–11] C–Mn steels,[6,7,12,13] and stainless steels.[5,14] Figure 2 shows a schematic drawing of the experimental setup where the focused synchrotron beam is passed through a monochromator before passing through a 540 μm diameter tungsten pinhole. This setup renders a ~600 μm diameter monochromatic beam on the sample at an incident angle of ~25°. The beam flux was measured to be $\sim 10^{12}$ photons/s as measured by an ion gauge detector placed immediately downstream from the 540 μm pinhole. The photon energy used for all the experiments was 12.0 keV ($\lambda = 0.1033$ nm).

One difference between the experiments presented here and those performed in the past is the intensity of the x-ray beam, which is nearly 2 orders of magnitude greater than before. This higher flux is the result of the recent installation of a liquid nitrogen-cooled monochronomator and a new x-ray focusing mirror on the beam-line. This increased flux provides higher quality diffraction peaks for a given pinhole size and counting time, enhancing peak profile analysis for more accurate measurements of the 2θ peak positions and peak shape determination.

The diffraction patterns were recorded using a 50 mm long, 2048 element position-sensitive Si photodiode array detector. This detector was placed ~100 mm behind the weld to cover a 2θ range from 22° to 52°. At 12.0 keV, this 2θ range covers three possible β-titanium peaks: bcc (110), bcc (200), and bcc(211); and 9 possible α-titanium (hcp) peaks. Figure 3 shows the ideal (powder pattern) calculated positions of the peaks in both phases at room temperature,[15] using lattice constants of $a = 0.330\,65$ nm for β (bcc), and $a = 0.295\,06$ nm, $c = 0.467\,88$ nm for α (hcp),[16] and compares these peaks with the 2θ range covered by the x-ray detector. In this diffraction pattern, the peak positions and intensities of pure titanium at room temperature and of each phase is assumed to be represented in roughly equal volume fractions. In the actual material alloying elements, as expected, alter the peak positions and the phase ratios from the calculated values.

Figure 4 shows one of the TRXRD patterns taken directly on the Ti–6Al–4V bar prior to welding. Since the alloy contains approximately 88% α at room temperature, the diffraction pattern is dominated by the hcp α diffraction peaks. All nine hcp peaks are present, in slightly different

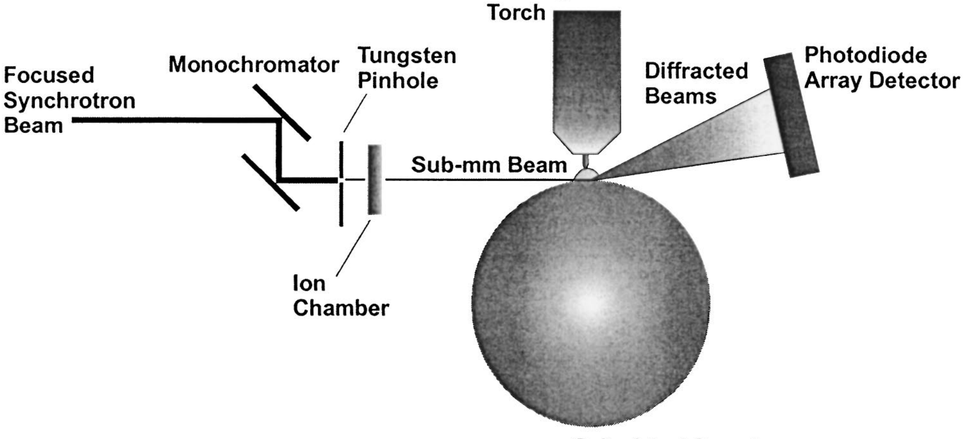

FIG. 2. Schematic drawing of the TRXRD setup used for *in situ* observations of phase transformations during welding.

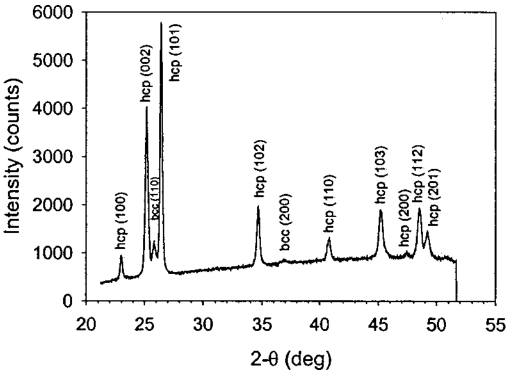

FIG. 4. Initial SRXRD diffraction pattern taken on the Ti–6Al–4V bar prior to welding. This pattern was acquired in 10 s, the same amount of time used during the welding experiments.

proportions to those calculated for powder diffraction due to texture in the starting material. The small amount of β phase in the starting microstructure diminishes the intensity of the β diffraction peaks, and only two of these peaks, bcc(110) and bcc(200), can be distinguished in the diffraction pattern at room temperature. The positions of the observed peaks have shifted from those calculated for pure titanium. For example, the bcc(110) has shifted to higher 2θ values relative to the hcp(002), and now appears directly between the hcp(002) and hcp(101) peaks at room temperature.

III. RESULTS

A. Phase equilibria

In Ti–6Al–4V, the V stabilizes the bcc crystal structure of the β phase, while the Al stabilizes the hcp crystal structure of the α phase. Two calculated pseudobinary diagrams for this alloy are shown in Fig. 5, one illustrating the influence of V on the α/β binary alloy equilibria, and the other illustrating the influence of Al on the α/β binary alloy equilibria. These calculations were performed using THERMOCALC[17] with the Ti-Data database (distributed by UES Software), by considering the influence of Ti, V, Al, Fe, and O on phase equilibria at the nominal alloy composition.

The phase relationships presented in Fig. 5 indicate that the amount of β phase will increase during heating, completely transforming to β at a temperature of 956 °C. Above this temperature, the β phase is stable up to the solidus temperature of 1693 °C, while complete melting occurs at the liquidus temperature of 1701 °C. These temperatures are slightly different than those published elsewhere based on experimental measurements,[2] where the liquidus is reported to be 1655 °C, the solidus to be 1605 °C, and the β transus to be 975 °C. In the results that follow, the experimentally determined values will be used here to represent the phase transformation temperatures, and THERMOCALC to illustrate compositional effects on phase stability.

The large difference in liquidus and β-transus temperature suggests that the liquid weld pool should be surrounded by a relatively large region of β that varies in size in response to varying temperature gradients around the weld pool. Outside of this single-phase β region, the α phase would be expected to coexist with β in varying amounts during welding, thus providing a transition to the reduced amount of β in the base metal. Since equilibrium is rarely attained during welding, the microstructures that form are often considerably different than those expected from the calculated phase diagram. Furthermore, the evolution of weld microstructures can be difficult to determine in titanium alloys using conventional techniques since the microstructures that form during heating are subsequently altered by the solid-state transformations that take place during cooling.

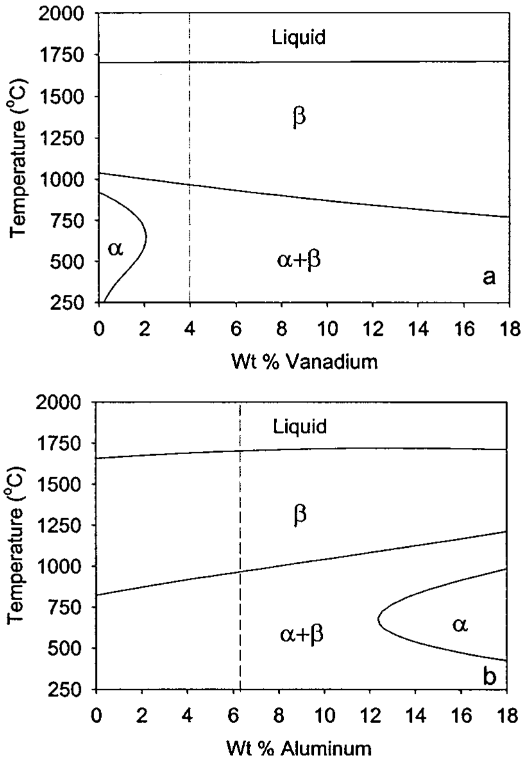

FIG. 5. Binary-alloy phase equilibrium calculated by THERMOCALC showing the influence of (a) the V content on the α and β phase equilibrium, and (b) the Al content on the α and β phase equilibrium. The vertical lines indicate the nominal V and Al contents of the alloy.

B. Weld microstructure

Figure 6(a) shows a cross section of one of the spot-welded samples to demonstrate the complexity of the Ti–6Al–4V weld microstructures. The fusion zone (FZ) is characterized by the appearance of large columnar grains that solidified as β and subsequently underwent a near-complete transition to a finely dispersed α or α' phase. The α' phase is a martensitic phase with an hcp crystal structure and similar lattice parameters to the α phase.[2] The FZ grains grew from the large β grains of the HAZ, where it is often difficult to distinguish the FZ and HAZ grains from each other. In this microstructure the HAZ/FZ boundary was revealed, using careful metallographic preparation techniques, as a dark etching line running through the columnar grains. This boundary is identified by the arrows in Fig. 6(a). It is clear that solidification occurred by epitaxial regrowth from the large HAZ grains. Outside the fusion zone, there is a gradient of prior β grain sizes extending from the HAZ/FZ boundary to the region of α/β coexistence. The region of coexistence

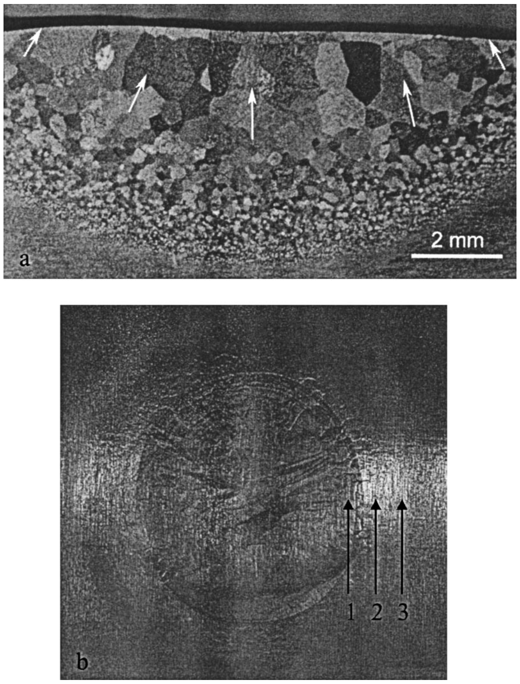

FIG. 6. (a) Metallographic cross section of the weld. The white arrows point to the fusion zone boundary. (b) Macrophotograph of the top surface of one of the welds indicating the relative positions of the three x-ray locations with respect to the fusion line.

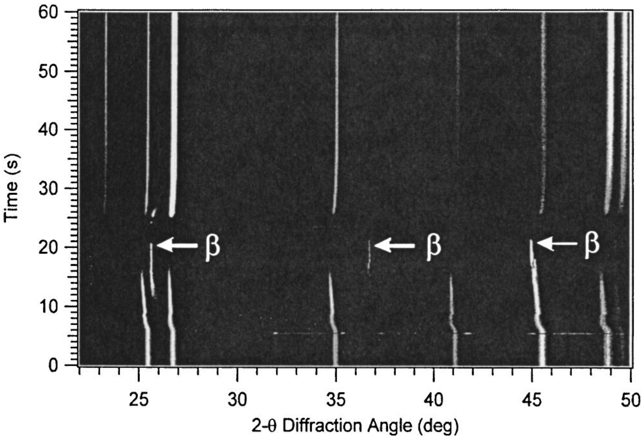

FIG. 7. Overview of the TRXRD diffraction patterns for weld 1. The arc was initiated at $t=5.8$ s, complete melting occurred at $t=23.8$ s, and solidification initiated at $t=25.1$ s. Complete transformation to β occurs at $t=17.8$ s, leaving only the three β peaks (indicated by arrows) present just before melting.

extends outward along the heat flow direction, reaching the unaffected base metal in the clearly defined semicircular cross-sectional boundary that measures approximately 6 mm from the center of the weld. This postweld characterization is useful in illustrating the final weld microstructure. However, it is not possible to reveal any information about the phase transition kinetics from the postweld microstructure alone.

C. Time-resolved x-ray diffraction

The locations where the TRXRD measurements were taken are shown in Fig. 6(b). Each TRXRD data set consisted of a series of 600 diffraction patterns taken at 100 ms intervals. This large amount of data is difficult to visualize in detail; however, it can be reproduced in different formats to illustrate the sequence of phase transformation events that take place during welding. One method to represent the data is to plot the data as a pseudocolor image, where the intensity of the color represents the intensity of the diffraction peaks.

Figure 7 plots the pseudocolor TRXRD data set for weld 1, which underwent melting and solidification. The 2θ locations of the peaks are plotted along the x axis, and weld time on the y axis. The seven prominent peaks at the beginning of the weld are all indexed to the α phase. The β peaks, although present, have too low an intensity to be visible in this pseudocolor overview at the beginning of the weld. After the arc is initiated at $t=5.8$ s (note the faint horizontal line caused when the arc was struck), these peaks move towards lower 2θ values due to thermal expansion. The α peaks decrease to zero intensity at $t=17.8$ s, leaving the three β peaks as indicated by the arrows. The intensity of the β peaks then decreases to zero as the alloy melts at $t=23.8$ s. The arc is extinguished at $t=25$ s (note faint horizontal line caused by the arc termination). Almost immediately the β phase appears, indicating β solidification from the melt. The β peaks only exist for a short time, and rapidly shift to higher 2θ values, indicating the cooling effect on the lattice parameter. Transformation to the α phase occurs rapidly, where eight prominent diffraction peaks from the α phase remain for the remainder of the experiment.

The TRXRD results of the other two experiments duplicate similar phase transformation progressions to that shown in Fig. 7. However, no melting was observed in these welds since the beam was located in the HAZ. In weld 2, the complete transformation to β was observed, and was accompanied by the complete disappearance of the hcp diffraction peaks. In weld 3 only partial transformation to β was observed, so both bcc and hcp diffraction peaks were present throughout the entire TRXRD run.

Analysis of every peak in each of the diffraction patterns was performed to estimate the relative fraction of the hcp and bcc titanium phases present as a function of weld time. To do this, the integrated intensity of each peak in each diffraction pattern was measured using a sum of one or more Gaussian peak profile fitting functions.[14] The area and FWHM values of the fitted peaks were then determined using an automated curve-fitting routine developed in IGOR PRO®, Version 4.0.[18]

Using the TRXRD measured areas of the x-ray diffraction peaks, the area fraction of the β peaks was calculated as the total area of the β peaks divided by the combined areas of the β and α peaks. Then, using the metallographically measured amount of β phase in the starting microstructure (12.1%) for calibration, the x-ray diffraction measurements of the β peak areas were converted into actual amount of the β phase throughout the TRXRD run. The fraction α was further calculated by subtracting the fraction β from unity, since only these two phases are present in the microstructure.

Each TRXRD run was analyzed using the integrated peak intensities to determine the fraction of the β phase as a

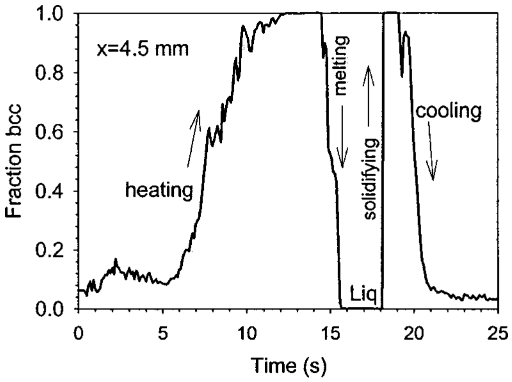

FIG. 8. Relative area fractions of the β phase in weld 1, where the beam was positioned 4.5 mm from the center of the weld. Melting and solidification was observed at this FZ location.

function of weld time. Figure 8 plots this result for weld 1, which underwent melting and solidification. In this plot, the time scale is set equal to zero at the point of arc initiation. The fraction of the β phase at this location remains at or about its base metal value for approximately 6 s, then begins to increase, and completely transforms to the β phase at $t = 13.5$ s. One second later, the β phase begins to melt and the sample is completely molten by $t = 15.7$ s. Solidification to the single-phase β begins rapidly after the arc is extinguished. The β phase is then stable for 0.9 s before the first appearance of α on cooling, and rapidly transforms to α/α' as the weld cools. The fraction β reaches its base metal value 1.9 s after the first α peaks were observed on cooling. Therefore, at this location, the complete $\alpha \rightarrow \beta \rightarrow \mathrm{L} \rightarrow \beta \rightarrow \alpha/\alpha'$ transformation sequence was observed during welding, and the changes in crystal structure were recorded with a time resolution of 0.1 s.

Similar plots are presented in Fig. 9 and Fig. 10 for the two HAZ weld locations. Figure 9 plots the β fraction versus time for weld 2, which underwent a complete transformation to β, but did not reach high enough temperatures to melt. The overall trend of increasing fraction of β with time is similar to that in weld 1. However, the complete transformation to β occurred later, requiring 16.7 s after arc initiation as compared to 13.5 s for weld 1. On cooling, the reverse transformation from β to its base metal required 4.2 s for this weld, which is longer than that of weld 1, which required only 1.9 s to take place. At the weld 3 location, which is shown in Fig. 10, the peak temperature was not high enough to completely transform the microstructure to β. The initial increase in β begins at $t = 9$ s, which is approximately 1 s later than that of weld 2, and 2 s later than that of weld 1.

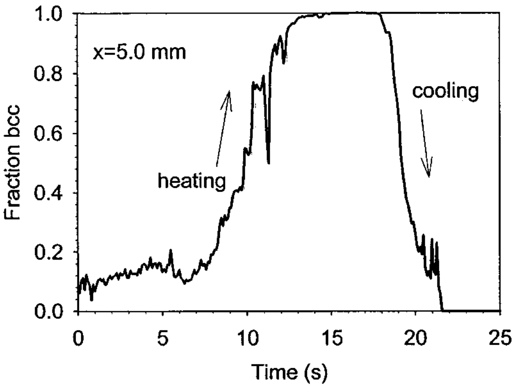

FIG. 9. Relative area fraction of the β phase in weld 2, where the beam was positioned 5.0 mm from the center of the weld. At this location, the HAZ underwent a complete transformation to the β phase.

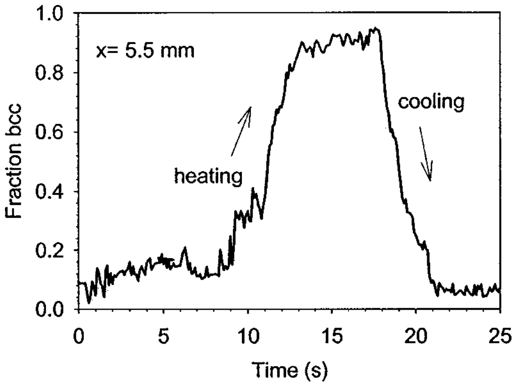

FIG. 10. Relative area fractions of the β phase in weld 3, where the beam was positioned 5.5 mm from the center of the weld. At this HAZ location only partial transformation to β was observed.

D. Coupled thermal-fluids numerical modeling

Whereas the TRXRD results presented in Figs. 8–10 show changes in the fraction β phase as a function of time, these data only provide limited information about the transformation kinetics since weld temperature has not yet been incorporated into the plot. In order to relate weld time to weld temperature, we use numerical modeling, since transient weld temperatures are extremely difficult to measure directly. The weld model used here is a well-tested 3D numerical heat transfer and fluid flow model as described in detail in Ref. 19 for a flat plate geometry. No significant error was introduced due to the heat transfer calculations in the flat geometry, since the weld pool dimensions were much smaller than the dimensions of the cylindrical bar. The weld pool boundary, i.e., liquid/solid interface, is traced using an enthalpy-porosity technique in a fixed Cartesian coordinate system.[19] The calculations take into account the electromagnetic, surface tension gradient, and buoyancy driving forces present in the transient weld pool convection, and also consider a variable arc efficiency for the first 2 s of arc on time as the arc establishes itself. In addition, at the weld top surface, the heat loss due to the helium shielding gas is considered by using Newton's law of cooling with an appropriate heat transfer coefficient, as summarized in the Appendix.[20–22]

For computational accuracy, a very fine grid system consisting of $110\times 55\times 48$ grid points was used, and the corresponding computational domain had dimensions of 92 mm long, 46 mm wide, and 32 mm deep. Spatially nonuniform grids were used for maximum resolution of the variables, such that the grid spacing was refined near the heat source where the temperature gradients are the highest. The minimum grid spacing along the x and z directions was about 100 and 10 μm, respectively. Small time steps of 0.1 s were

TABLE III. Physical properties of Ti–6Al–4V used in the weld heat flow calculations.

Physical property	Value
Liquidus temperature, T_L (K)	1928
Solidus temperature, T_S (K)	1878
Density of liquid metal, ρ (kg/m^3)	3.89×10^3
Effective viscosity of liquid, μ (kg/m-s)	0.049
Thermal conductivity of liquid, k_L (W/m-K)	32.5
Thermal conductivity of solid, k_S (W/m-K)	8.3 to 24.2
Specific heat of solid, C_{PS} (J/kg-K)	725
Specific heat of liquid, C_{PL} (J/kg-K)	872
Temperature coefficient of surface tension, $d\gamma/dT$ (N/m-K)	-2.8×10^{-4}
Coefficient of thermal expansion (K^{-1})	1.1×10^{-5}
Convective heat transfer coefficient top surface (W/m^2-K)	1.59×10^3

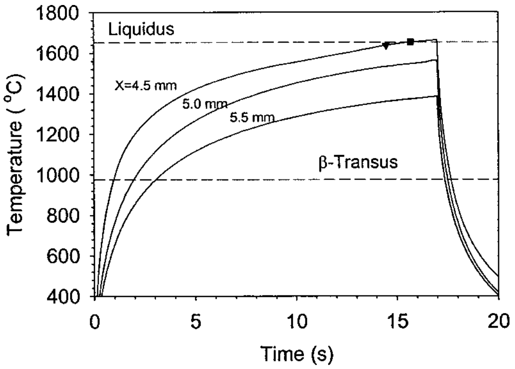

FIG. 11. Results of the coupled thermal–fluids model showing the calculated weld thermal cycles at the three x-ray locations. The triangle marks the TRXRD time where melting was observed to begin, and the square where melting was observed to be complete.

further required to track the weld pool size and shape under the high heating and cooling rates produced under the transient welding conditions.[19]

The thermophysical properties used to represent the Ti–6Al–4V alloy in the calculations are given in Table III.[23,24] It should be noted that the specific heat (C_P), thermal conductivity (k), and density (ρ) of Ti–6Al–4V vary with temperature.[23] Hence, accurate calculations of weld temperature need to consider the temperature dependence of these properties. However, if the C_P, k, and ρ are all taken as temperature dependent, the computational task is very difficult. Therefore, in the present calculations, only k is treated as temperature dependent, while C_P and ρ are assumed to be constant. This approach largely simplifies the model, while still preserving significant accuracy since these thermophysical properties are of importance in their combined form, i.e., $k/(\rho,C_P)$. For the Ti–6Al–4V alloy, the thermal conductivity of solid increases from 8.3 W/m-K at 300 K to 24.2 W/m-K at 1900 K.

The cross-sectional shape of the calculated weld pool at its maximum size matched the experimental weld cross section having a width just under 10 mm and a maximum depth of 1.3 mm. Using the results from the weld model, the temperature distributions, heating rates, and cooling rates are calculated as a function of welding time at each TRXRD location. The calculated weld time–temperature plots for each of the three x-ray locations are shown in Fig. 11, and are compared to the calculated liquidus temperature of the Ti–6Al–4V alloy. It is clear that the monitoring location closest to the center of the weld heated the fastest, and is the only location of the three to reach the liquidus temperature. The other two x-ray locations have temperatures that exceed the β transus temperature and are held above this temperature for times in excess of 10 s prior to extinguishing the arc. In this figure, the symbols mark the times where the TRXRD measurements showed that the melting began (triangle), and where melting was complete (square).

IV. DISCUSSION

The calculated α/β phase equilibria indicated that the fraction of the β phase will reach unity at the β transus temperature. This relationship can be explored more closely by using the thermodynamic software to calculate the equilibrium volume fraction of β as a function of temperature. These results are plotted in Fig. 12, which shows that the fraction of β is relatively constant, at about 4%, up to a temperature of approximately 450 °C. In fact, the calculations predict a slight dip in the fraction of β, due to the retrograde in the α phase field as shown in Fig. 5. Above 450 °C, the β fraction increases at an increasing rate, until complete transformation occurs at the β transus.

The calculated β fraction, which is plotted versus temperature in Fig. 12, has a similar shape to that of the heating stages of the TRXRD measurements shown in Figs. 8–10. In these figures, the β content is relatively low and constant during the initial heating stages, but then rapidly increases at higher temperatures. However, the nonuniform weld heating rate, indicated in Fig. 11, needs to be considered in order to better compare the TRXRD measurements with the thermodynamic predictions.

The weld temperature not only influences the α/β phase ratio, but also the individual compositions of the α and β phases. Variations in the composition of these phases are predicted with thermodynamic calculations, as illustrated in

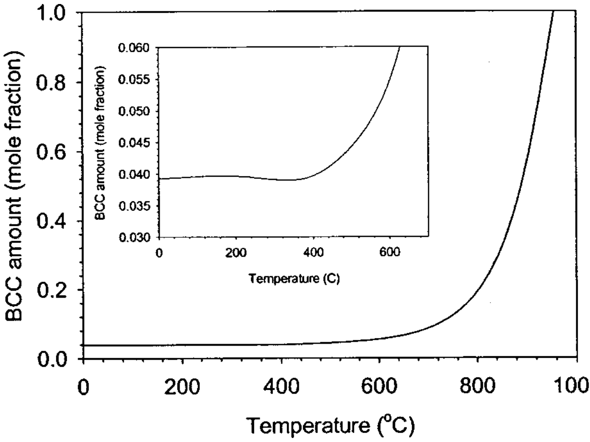

FIG. 12. THERMOCALC results plotting the equilibrium fraction β (bcc) versus temperature. The inset plot shows the low-temperature behavior and indicates a slight dip in β around 400 °C.

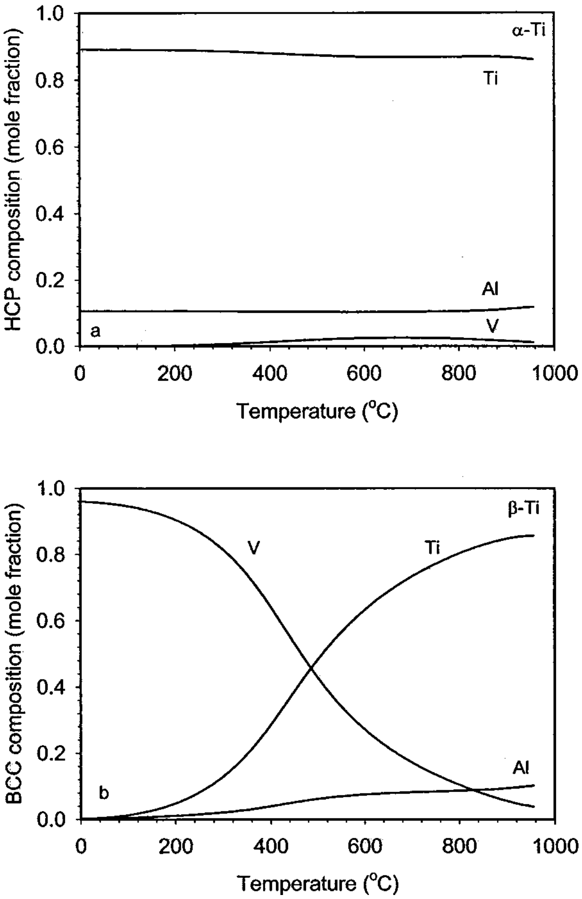

FIG. 13. THERMOCALC results showing the V, Ti, and AL content of (a) the α phase and (b) the β phase as a function of temperature.

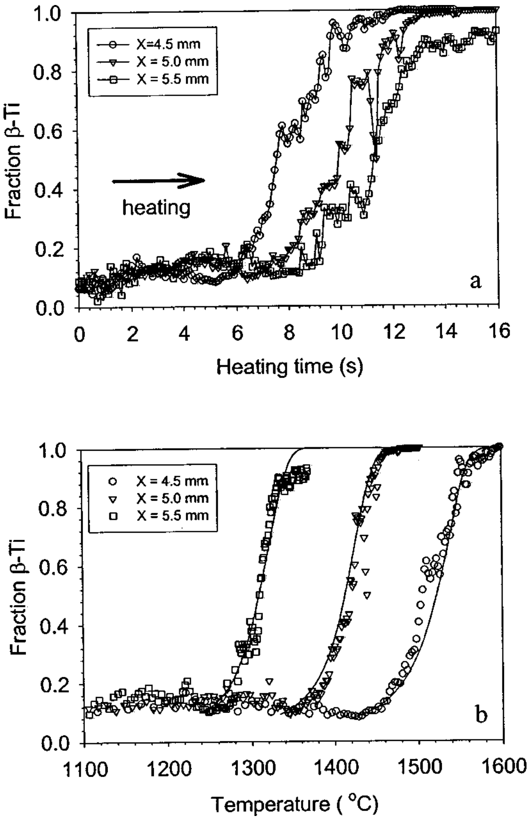

FIG. 14. TRXRD results showing fraction β during the heating cycle of the weld plotted versus (a) weld time after arc is on, and (b) weld temperature, where the solid lines mark the JMA fit to the data using a fixed value of $n=4.0$.

Fig. 13. These results show that the composition of the α phase changes very little over the entire temperature range up to the β transus temperature. However, the β phase shows a dramatic variation in composition, whereby V concentrates strongly during cooling. The reason for this behavior is related to the solubility of V in the α phase, which is small and relatively constant. Therefore, as the alloy transforms from $\beta \rightarrow \alpha$ as the temperature decreases, the V concentration in β increases dramatically to accommodate nearly all of the V into the smaller and smaller volume fraction of the remaining β.

A. Transformation kinetics during weld heating

The fraction of β versus weld temperature can be determined by combining the calculated thermal profiles with the TRXRD integrated peak area analyses. This correlation was performed and the results are illustrated in Figs. 14(a) and (b), which replot the fraction of β measured in the TRXRD experiments as a function of weld time and weld temperature, respectively. In these figures, the data for the three TRXRD locations are represented by the symbols, and kinetic modeling results are shown by the solid lines. The modeling results are discussed in more detail later. The data plotted versus weld time in Fig. 14(a) show that the transformation follows a general sigmoidal shape at each location. More rapid heating and higher transformation rates occur at the locations closest to the center of the weld, when the microstructure is completely transformed to β.

Figure 14(b) shows these same data plotted versus temperature. Here, locations farther from the center of the weld transform at lower temperatures. This fact is related to the time–temperature kinetics of the $\alpha \rightarrow \beta$ phase transformation, whereby higher amounts of superheat are required at locations closer to the weld center where the heating rates are higher.

The kinetics of the $\alpha \rightarrow \beta$ phase transformation at each location was modeled using the Johnson–Mehl–Avrami (JMA) approach to develop a set of parameters that could be used to predict the extent of the phase transformation for different weld heating rates. The JMA approach is represented by the following expression:[25]

$$f_e(t) = 1 - \exp\{-(kt)^n\}, \tag{1}$$

where $f_e(t)$ is the extent of the transformation at a given time t, n is the JMA exponent, and k is a rate constant, given as

$$k = k_0 \exp\left(-\frac{Q}{RT}\right), \tag{2}$$

where k_0 is a pre-exponential constant, Q is the activation energy of the transformation including the driving forces for both nucleation and growth, R is the gas constant, and T is the absolute temperature.

TABLE IV. Summary of the calculated JMA parameters for each of the weld locations, using two different assumptions about the dominant phase transformation mechanism. The underlined values of n and Q indicates the parameters that were held constant for the calculations.

Location	n	$\ln(k_0)$	Q (kJ/mol)	Average error
$X=4.5$ mm	*4*	8.2	144	0.0425
	6.3	6.4	*123.9*	0.0448
$X=5.0$ mm	*4*	11.2	186	0.0640
	10.5	5.8	*123.9*	0.0646
$X=5.5$ mm	*4*	12	188	0.0635
	8.8	6.4	*123.9*	0.0645
All data	*4*	11.4	189	0.0547
	6.4	6.25	*123.9*	0.0647

Although the activation energy of phase transformations occurring under isothermal conditions is often known, the overall activation energy under nonisothermal welding conditions is rarely known when nucleation and growth are simultaneously operating. This is because the contributions of nucleation to the overall activation energy are temperature and rate dependent,[26] and are further influenced by the starting microstructure.[25] Thus, a unique activation energy for the overall transformation is not always possible to determine. However, if a given transformation has a large growth component, it may be treated as a growth-controlled mechanism, and the activation energy for growth provides a reasonable starting assumption.

Equations (1) and (2) were discretized and numerically integrated over the nonisothermal heating profile of the weld following a previously developed procedure whereby transformation in a two-phase field can be taken into account.[12] To do this, the TRXRD data were fit using the JMA parameters (n, ko, and Q), by selecting one of the JMA parameters and calculating the remaining two using a numerical data fitting procedure.[13]

In the first calculation, the activation energy for the diffusion of V is used to represent a growth-controlled phase transformation mechanism where nucleation is assumed not to play a significant role.[26] Since the V content of the α phase is nearly constant up to the β transus temperature, V diffusion in α will not be a rate controlling factor. Instead, the transport of V through the β phase will control the transformation rate, assuming the interface mobility of the α/β interface is high.[26] The diffusion coefficient for V in the β phase can be represented by an Arhennius expression, $D=A\exp(-Q/RT)$, and has been measured to have an activation energy $Q=123.9$ kJ/mole, with a pre-exponential of $A=1.6\times10^{-4}$ cm^2 s^{-1} for a binary Ti–V alloy containing 10 a/oV.[24]

The optimum JMA parameters (n and ko) for the diffusion-controlled growth assumption with an activation energy of $Q=123.9$ kJ/mole were calculated by minimizing the error between the JMA fit and the TRXRD data at each weld location. The results are summarized in Table IV, showing that the average error between the fit and the data points is small for all cases. The calculated ln(ko) values varied between 5.8 and 6.4. The n values varied from 6.3 to 10.5. Even though the JMA fit to the data is good in all cases, the calculated n values are higher than expected for a diffusion-controlled growth transformation, where a value of $n\leqslant 4.0$ would be considered to be representative.[25]

The calculations were then performed using a different set of assumptions where nucleation and growth would simultaneously occur. This time, a reasonable value of $n=4$ was selected for a transformation mechanism that involves a strong nucleation component.[25] Using this assumption, ko and Q were calculated using the same JMA modeling approach. The reasoning here is that although the activation energy for growth is temperature independent, the activation energy for nucleation is temperature dependent,[27] and therefore the combination of the two may result in an activation energy different than either one alone. The results of these calculations are also summarized in Table IV, showing again that the average error between the fit and the data points is small for all cases, and better than the previous fits where Q was held constant. This time the ln(ko) values varied between 8.2 and 12.0, increasing with distance from the center of the weld. The calculated activation energy for the transformation varied from 144 to 188 kJ/mole, increasing with distance from the center of the weld. The results of these calculations are superimposed as the solid lines over the measured fraction of β versus time and temperature plots shown in Fig. 14(b), illustrating the good data fit in all three cases.

The range in JMA parameters for the three data sets is reasonably small, suggesting that the same phase transformation mechanism may be operating at each location. Therefore, it is possible to optimize all of the data sets together to produce one set of JMA parameters to represent the transformation. The results of this calculation are also summarized in Table IV for both the $n=4$ assumption and the $Q=123.9$ kJ/mole assumption. The fit to the data is better for the $n=4$ assumption, which results in an overall activation energy $Q=189$ kJ/mole and a corresponding value of ln(ko)$=11.4$.

To summarize the results of the JMA calculations, two different starting assumptions led to different values for the activation energy for the transformation. The difficulties associated with using the JMA approach to determine activation energies for transformations involving nucleation and growth have been observed by other investigators,[28] and additional studies will be required to provide more conclusive evidence for the transformation mechanism during transient weld heating of Ti–6Al–4V. However, the JMA modeling approach did successfully produce sets of parameters ($Q=189$ kJ/mole, $n=4.0$, and ln(ko)$=11.4$) that allow the weld heating transformation rate to be predicted, even though the transformation mechanism was not definitively established.

B. Transformation kinetics during weld cooling

Once the arc is extinguished, the weld cools rapidly and β begins to transform to α/α'. The $\beta\rightarrow\alpha$ transformation on cooling have several differences from the $\alpha\rightarrow\beta$ transformation on heating. The temperature profiles plotted in Fig. 11 show that the heating rates at the β transus temperature vary from 120 to 360 °C/s, whereas the cooling rates vary from 1430 °C/s to 2000 °C/s at the time the arc is terminated to 530 °C/s at the β transus temperature.

The second difference relates to the nature of the microstructures at each of the three weld locations. Weld 1, closest to the center of the weld, undergoes melting and solidification to β prior to beginning the $\beta \rightarrow \alpha$ transformation on cooling. Thus, the microstructure is composed entirely of large columnar β grains that formed during solidification, and would require nucleation of the α phase before transformation can begin. Weld 2, in the hottest portion of the HAZ, underwent a complete transformation to β and experienced grain growth at these elevated temperatures. The resulting microstructure is therefore also composed entirely of large β grains and would require nucleation of the α phase before transformation can begin. However, the nucleation conditions would most likely be different at these locations because the grain growth and chemical homogenization that occurs in the HAZ is different than what occurs during solidification. Weld 3, the furthest from the center of the weld, never transformed completely to β, and therefore contains a mixture of α and β at the time when the reverse transformation to α begins. Therefore, this location would not require nucleation of α prior to the $\beta \rightarrow \alpha$ transformation. Thus, the difference in microstructures, combined with the high cooling rates, should lead to different transformation kinetics on cooling than on heating.

The results of the TRXRD measurements showing the fraction of β during weld cooling time are plotted in Fig. 15(a), where time equal to zero represents the time when the arc was extinguished. In this figure, the amount of β versus cooling time is plotted for each of the three locations. At the location furthest from the weld center, the amount of β shows an overall increase after the arc is extinguished. This behavior is the result of the incomplete transformation to β and the fact that the temperature is still above the β transus for some time after the arc is turned off. Thus, even though the weld is cooling, the $\alpha \rightarrow \beta$ transformation continues for approximately 0.5 s. The transformation to α then commences, and the β content decreases nearly to zero, approximately 4 s after the arc has been extinguished. Weld 2, in the HAZ adjacent to the fusion boundary, maintains 100% β for nearly 1 s after the arc has been extinguished, before beginning to transform to α. Nearly complete transformation to α occurs at this location approximately 3 s after the arc was extinguished. Weld 1, closest to the center of the weld, is liquid when the arc is extinguished, and continues to be molten for approximately 1 s prior to solidifying completely to the β phase. The β is stable for approximately 1 s before beginning to transform to α/α'. This transformation reaches completion approximately 3.5 s after the arc has been extinguished.

These data are further plotted in Fig. 15(b) as a function of the calculated weld temperature. This figure shows that the $\beta \rightarrow \alpha$ transformation begins at a different temperature at each location. In the two HAZ locations, the reverse transformation to α/α' occurs at, or very near, the β transus temperature. However, for the location in the FZ, the transformation is first observed at 600 °C, which corresponds to approximately 375 °C of undercooling below the β transus, and is also below the Ms temperature.

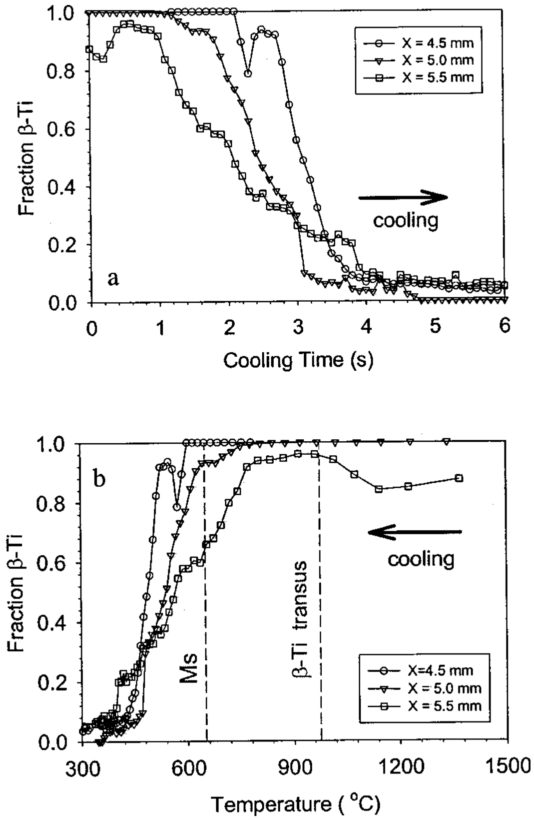

FIG. 15. TRXRD results showing fraction β during the cooling cycle of the weld plotted versus (a) weld time after arc is off and (b) weld temperature. The vertical dashed lines mark the calculated α/β transus, and the approximate Ms temperature for this alloy.

The transformation kinetics at each location varies significantly, and does so in response to the different microstructures that evolved at these different locations during the heating cycle of the weld. The location showing the most transformation at temperatures close to the β transus is the location furthest from the center of the weld. Since both α and β are present in the microstructure no nucleation is required, and the transformation quickly commences as the temperature falls below the β transus.

The next HAZ region, which is closer to the center of the weld at monitoring location 2, completely transformed to β during heating, and experienced grain growth prior to the back transformation to α during weld cooling. Here, the transformation began at the β transus, but did so very slowly, which may be an indication that nucleation of α was required. Note again that the transformation appears to arrest at a β fraction of approximately 0.9 before commencing again on further cooling.

The location in the FZ showed significant undercooling prior to beginning the back transformation to α/α'. At this location, which has the largest β grains, the undercooling below the β transus was measured to be 375 °C before the presence of α/α' was detected at approximately 3.5 s after the β transus was reached. Again, an arrest in the transformation was observed at a β fraction of approximately 0.9 before commencing again on further cooling

Qualitatively, the decreasing amounts of transformation at a given temperature at locations closer to the center of the weld are expected from nucleation and growth theory. Quantitatively, this behavior is more difficult to describe due to the multiple changes associated with the different thermal and microstructural histories at each location. Experiments and modeling of the $\beta \rightarrow \alpha$ phase transformation in Ti–6Al–4V have been performed to better understand the individual roles of nucleation and growth at different cooling rates.[27] Katzov *et al.* showed that the thickness of the α lamella decreased with increasing cooling rate, and the amount of transformation that occurred at a given temperature decreased with increasing cooling rate.[27] These facts were related to the decrease in the temperature where the peak nucleation rate occurs and to the reduced time for the $\beta \rightarrow \alpha$ phase transformation to take place as the cooling rate was increased. Their work was performed at much lower cooling rates than those experienced by the welds in this investigation, and for a growth-controlled transformation to the α phase. However, there is a high likelihood that α' martensite is forming in the high cooling rate welds produced in this study.

The microstructures of the weld are shown in Fig. 16 at the three locations representative of where the x-ray diffraction measurements were taken. The microstructures show the presence of α' martensite with its characteristic needle-shaped morphology.[2] This microstructure forms when untransformed β is subjected to temperatures below the martensite start temperature (Ms) on cooling. The Ms temperature for Ti–6Al–4V is approximately 650 °C,[2] but varies with chemical inhomogeneity of the β phase. Although each location contains α' martensite, the amount and distribution differ at each location. Figure 16(a) shows the microstructure at location 1 in the FZ. At this magnification, the microstructure appears to be composed entirely of α' martensite, where the length of many of the needles exceeds 100 μm. This microstructure has no obvious signs of retained β, and appears to form entirely through the diffusionless martensitic mechanism. This microstructure is consistent with the TRXRD data and the computed temperatures, showing that all of the transformation occurred below the Ms temperature.

The microstructures at the HAZ locations contain some features not present in the FZ. The microstructure of weld location 2 is shown in Fig. 16(b) and contains a dark etching phase between some of the α' martensite needles. This dark etching phase is presumably retained β, and the patches seen in the upper left-hand side of the micrograph are on the order of 10 μm. Figure 16(c) shows the microstructure of weld location 3, which also contains retained β phase, but in higher amounts than at weld location 2. In places, the elongated patches of retained β reach lengths of nearly 100 μm, while never exceeding 10 μm in thickness. Another difference between this microstructure and the previous microstructures is the length of the α' martensite needles, which are shorter at this location than at the other locations. The reason for the reduced length of the α' martensite needles is most likely the presence of α at the time when β began its back transformation on cooling in this partially transformed region of the HAZ. The presence of α in the incompletely transformed microstructure may inhibit growth of α' martensite needles.

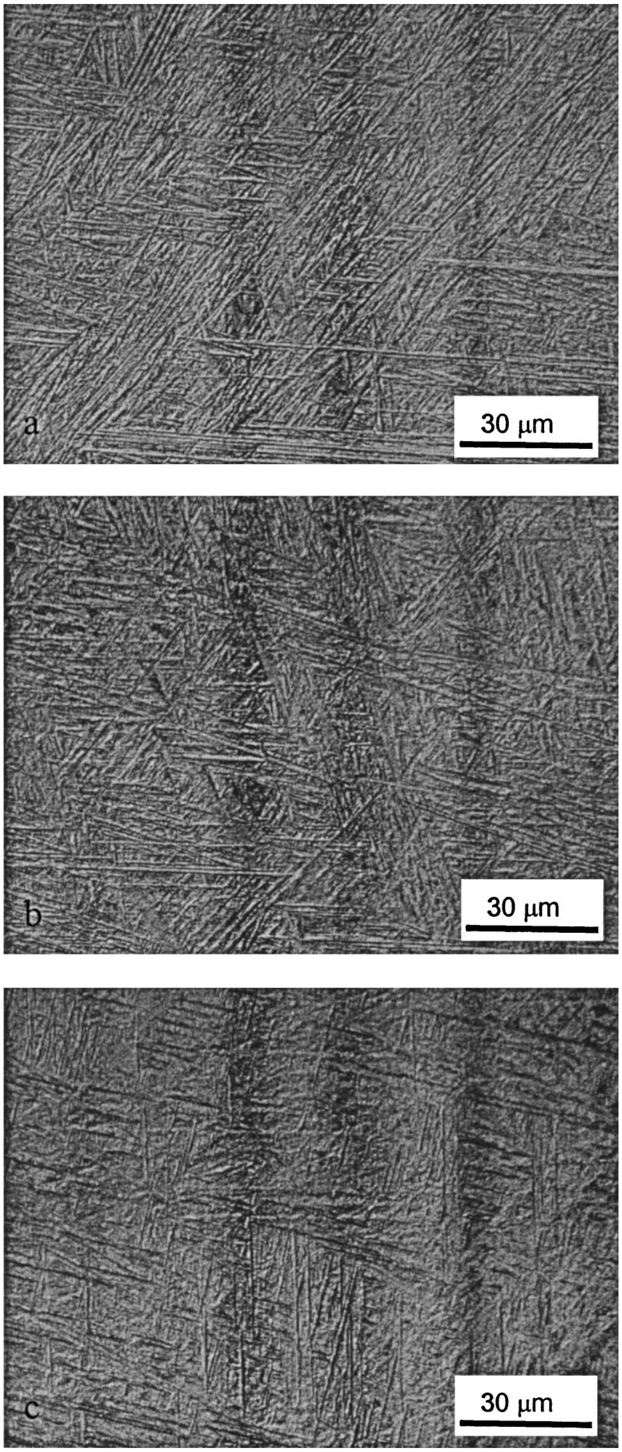

FIG. 16. High magnification micrographs taken of the weld microstructure at each of the three locations. (a) weld 1 fusion zone, 4.5 mm from weld center; (b) weld 2 HAZ, 5.0 mm from weld center; and (c) weld 3 HAZ, 5.5 mm from weld center.

The microstructures presented in Figs. 16(a)–(c) show a decrease in the martensite content as the distance from the center of the weld increases. The decreasing amount of martensite with distance is consistent with the TRXRD observations, whereby transformations in the FZ took place entirely

TABLE V. Data used in the calculation of heat transfer coefficient by forced convection of the helium shielding gas.

Properties	Value
T_{av}	1200 K
Density, ρ	0.1785 kg m^{-3}
Viscosity, μ	4.86×10^{-5} kg m^{-1} s^{-1} (4.86×10^{-4} g cm^{-1} s^{-1})
Specific heat, C_p	520 J kg^{-1} K^{-1}
Thermal conductivity, k	0.376 J m^{-2} s^{-1} K^{-1} (8.98×10^{-4} cal cm^{-2} s^{-1} K^{-1})
Gas flow rate, Q_g	1.02×10^{-3} m^3 s^{-1} (130 ft^3 h^{-1})
Nozzle diameter, d	3.175×10^{-3} m (0.125 in.)
Gas flow velocity, u	129.1 m s^{-1}
Diameter of the workpiece, l	0.114 m
Re	1505
Pr	0.067

below the Ms temperature of the alloy. In the HAZ locations, TRXRD showed that the $\beta\rightarrow\alpha$ transformation initiated at the β transus, but completed below the Ms temperature. This is also consistent with the metallographic observations. Additional work needs to be performed to see if the TRXRD transformation curves can be correlated to changes in the transformation mechanisms, and if specific kinetic data can be extracted from these measurements.

V. CONCLUSIONS

(1) TRXRD experiments employing synchrotron radiation were performed *in situ* on transient GTA welds on Ti–6Al–4V alloys, providing real-time observations of the $\alpha\rightarrow\beta\rightarrow L\rightarrow\beta\rightarrow\alpha/\alpha'$ phase transformation sequence in both the weld FZ and HAZ.

(2) A 3D transient numerical weld model was used to predict weld temperatures as a function of weld time and location. The model calculated the evolution of the FZ velocity fields and temperatures, and was validated by comparing the predicted and experimentally measured geometry of the FZ.

(3) During weld heating, the TRXRD measurements showed that the $\alpha\rightarrow\beta$ transformation took place above the β transus temperature with significant superheat required for completion due to the rapid heating rate of the weld. Decreasing amounts of superheat were required at distances further from the weld center due to the corresponding decrease in heating rates.

(4) The kinetics of the $\alpha\rightarrow\beta$ transformation on heating were modeled using a modified JMA approach using different assumptions about the mechanisms for nucleation and growth. These results produced a set of JMA parameters for the prediction of the transformation rate [$Q=189$ kJ/mole, $\ln(ko)=11.4$, $n=4.0$], but were not successful in determining a definite mechanism for the overall transformation.

(5) During weld cooling in the HAZ, TRXRD measurements showed that the $\beta\rightarrow\alpha$ transformation initiated at the β transus temperature, but completed the transformation below the Ms temperature. The transition from $\beta\rightarrow\alpha$ to $\beta\rightarrow\alpha'$ appeared to take place after approximately 5%–10% of the microstructure had initially transformed to α in both the partially transformed and the completely transformed regions of the HAZ.

(6) During weld cooling in the FZ, TRXRD measurements showed that the initiation of the $\beta\rightarrow\alpha'$ transformation began at temperatures at or below the Ms temperature. Once initiated, the transformation occurred rapidly and nearly completely to α' martensite in less than 2 s over a temperature range of approximately 200 °C.

ACKNOWLEDGMENTS

This work was performed under the auspices of the U.S. Department of Energy, Lawrence Livermore National Laboratory, under Contract No. W-7405-ENG-48, and the LLNL portions of this work were supported by D.O.E., Office of Basic Energy Sciences, Division of Materials Science. Part of the research was sponsored by the U.S. Department of Energy Division of Materials Sciences and Engineering under Contract No. DE-AC05-00OR22725 with UT-Battelle, LLC. Portions of this research were also carried out at the Stanford Synchrotron Radiation Laboratory, a national user facility operated by Stanford University on behalf of the U.S. Department of Energy, Office of Basic Energy Sciences. The authors express gratitude to Mr. Bob Vallier of LLNL for performing optical metallography, and Mr. Octavio Cervantes for performing x-ray diffraction simulations using JADE software.

APPENDIX: EFFECT OF SHIELDING GAS ON SURFACE TEMPERATURE DURING THE TRXRD EXPERIMENTS

Helium gas was used to shield the area where the TRXRD measurements were being taken to eliminate the deposition of metallic particles. This cross jet of helium gas created an additional cooling effect on the surface of the weld. The cooling effect of the shielding gas was studied by considering heat transfer by forced convection, as the helium shielding gas impinges on the location where the x-ray beam is located. Table V summarizes the parameters and properties of the helium gas used in the experiments for the helium flow rate of 130 ft^3/h.

The effect of the shielding gas on the surface temperature was calculated by considering the convective heat transfer between the workpiece and surrounding gas, as given in the following equation:[20]

$$F_c = -h_c(T_s - T_g), \tag{A1}$$

where F_c is the heat flux ($\mathrm{J\,m^{-2}\,s^{-1}}$), T_s and T_g are surface and gas temperatures (K), respectively, and h_c is the heat transfer coefficient ($\mathrm{J\,m^{-2}\,s^{-1}\,K^{-1}}$).

In order to use Eq. (A1) to calculate the convective heat loss at the weld top surface, the knowledge of heat transfer coefficient (h_c) is required. In general, the value of h_c depends on the geometry of the system, the location along the surface, the fluid velocity, and the properties of the fluid. The heat transfer coefficient for a particular situation can be obtained either by direct measurement or from existing empirical or semiempirical correlations. Some commonly used correlations are summarized in Ref. 20.

The shielding gas flowed in the tangential direction to the workpiece top surface. Thus, the following equation for a gas jet impinging on a solid surface[21] is used:

$$h_c = \frac{002k\,\mathrm{Re}^{0.87}\mathrm{Pr}^{0.33}}{l}, \tag{A2}$$

where l is the diameter of the workpiece (m), k is the thermal conductivity of shielding gas ($\mathrm{J\,m^{-2}\,s^{-1}\,K^{-1}}$) at temperature T_{av}, which is the arithmetic average of T_l (liquids temperature) and T_g, Re is the Reynolds number at the nozzle exit, and Pr is the Prandtl number. The Reynolds number and Prandtl number are given by the following equations:

$$\mathrm{Re} = \frac{\rho u d}{\mu} = \frac{4\rho Q_g}{\pi \mu d} \tag{A3a}$$

$$\mathrm{Pr} = \frac{C_p \mu}{k}, \tag{A3b}$$

where ρ, μ, and C_p are the density, viscosity, and specific heat of the shielding gas, respectively, u is the velocity of the shielding gas at the nozzle exit, and Q_g is the flow rate of the shielding gas. Using the data given in Table V, the heat transfer coefficient is found to be 0.038 $\mathrm{cal\,m^{-2}\,s^{-1}\,K^{-1}}$.

It should be noted that the heat transfer coefficient at the top surface may be a function of distance from the nozzle center. In other words, directly under the nozzle, the heat transfer coefficient should be a maximum, while far away from the nozzle the heat transfer coefficient should be insignificant. Accurate determination of the spatial variation of heat transfer coefficient is difficult; therefore, a constant heat transfer coefficient was assumed to be valid across the entire top surface of the bar.[22]

[1] M. Donachie, Jr., *Titanium A Technical Guide* (ASM International, Metals Park, OH, 1989).

[2] *Material Properties Handbook: Titanium Alloys* (ASM International, Metals Park, OH, 1994).

[3] *ASM Handbook, Volume 6: Welding, Brazing and Soldering* (ASM International, Metals Park, OH, 1993).

[4] Ø. Grong, *Metallurgical Modelling of Welding* (The Institute of Materials, London, 1994).

[5] J. W. Elmer, J. Wong, and T. Ressler, Scr. Mater. **43**, 751 (2000).

[6] S. S. Babu, J. W. Elmer, S. A. David, and M. Quintana, "*In-Situ* Observations of Non-equilibrium Austenite Formation During Weld Solidification of a Fe–C–Al–Mn Low Alloy Steel," in Proceedings of the Royal Society: Mathematical, Physical, and Engineering Sciences, 458, pp. 811–821 (2002).

[7] J. Wong, T. Ressler, and J. W. Elmer, J. Synchrotron Radiat. **10**, 154–167 Part 2 Mar (2003).

[8] V. Karpenko *et al.*, Rev. Sci. Instrum. **60**, 1451 (1989).

[9] J. W. Elmer, J. Wong, and T. Ressler, Metall. Mater. Trans. A **29A**, 2761 (1998).

[10] J. W. Elmer, T. A. Palmer, and J. Wong, J. Appl. Phys. **93**, 1941 (2003).

[11] Z. Yang, J. W. Elmer, J. Wong, and T. DebRoy, Weld. J. (Miami, FL, U. S.) **79**, 97 (2000).

[12] J. W. Elmer, J. Wong, and T. Ressler, Metall. Mater. Trans. A **32A**, 1175 (2001).

[13] J. W. Elmer, T. A. Palmer, W. Zhang, B. Wood, and T. DebRoy, Acta Mater. **51**, 3333 (2003).

[14] T. A. Palmer, J. W. Elmer, and J. Wong, Sci. Technol. Weld. Joining **7**, 159 (2002).

[15] JADE, *version 6.0*, Materials Data Inc., Livermore, California, 2001.

[16] C. Barrett and T. Massalski, *Structure of Metals*, 3rd ed. (Pergamon, New York, 1982).

[17] B. Sundman, B. Jansson, and J. Andersson, CALPHAD: Comput. Coupling Phase Diagrams Thermochem. **9**, 153 (1985).

[18] S. S. Babu, Private communications, Oak Ridge National Laboratory, 2002.

[19] W. Zhang, G. G. Roy, J. W. Elmer, and T. DebRoy, J. Appl. Phys. **93**, 3022 (2003).

[20] R. B. Bird, W. E. Stewart, and E. N. Lightfoot, *Transport Phenomena* (Wiley, New York, 1994), p. 391.

[21] J. Szekely and N. J. Themelis, *Rate Phenomena in Process Metallurgy* (Wiley, New York, 1971), Chap. 8.3.

[22] G. C. Huang, J. Heat Transfer **85**, 237 (1963).

[23] K. C. Mills, *Recommended Values of Thermophysical Properties for Selected Commercial Alloys* (ASM International, Metals Park, OH, 2002).

[24] C. J. Smithells, E. A. Brandes, and G. B. Brook, *Smithells Metal Reference Book*, 7th ed. (Butterworth-Heinemann Ltd., Oxford, United Kingdom, 1992).

[25] J. W. Christian, *The Theory of Transformations in Metals and Alloys*, 2nd ed., (Pergamon, Oxford, 1975), Part I.

[26] S. Malinov, Z. Guo, W. Sha, and A. Wilson, Metall. Mater. Trans. A **32A**, 879 (2002).

[27] I. Katzov, S. Malinov, and W. Sha, Metall. Mater. Trans. A **33**, 1027 (2002).

[28] M. B. Berkenpas *et al.*, Scr. Metall. **20**, 323 (1986).